

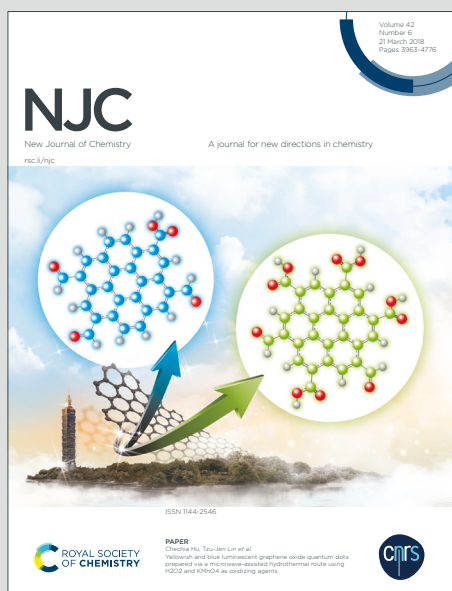
NJC

New Journal of Chemistry

Accepted Manuscript

A journal for new directions in chemistry

This article can be cited before page numbers have been issued, to do this please use: K. K. Haldar, R. Biswas, A. Kundu, M. Saha, V. Kaur, B. Banerjee, R. S. Dhayal, R. Patil, Y. Ma and T. Sen, *New J. Chem.*, 2020, DOI: 10.1039/D0NJ01596B.



This is an Accepted Manuscript, which has been through the Royal Society of Chemistry peer review process and has been accepted for publication.

Accepted Manuscripts are published online shortly after acceptance, before technical editing, formatting and proof reading. Using this free service, authors can make their results available to the community, in citable form, before we publish the edited article. We will replace this Accepted Manuscript with the edited and formatted Advance Article as soon as it is available.

You can find more information about Accepted Manuscripts in the [Information for Authors](#).

Please note that technical editing may introduce minor changes to the text and/or graphics, which may alter content. The journal's standard [Terms & Conditions](#) and the [Ethical guidelines](#) still apply. In no event shall the Royal Society of Chemistry be held responsible for any errors or omissions in this Accepted Manuscript or any consequences arising from the use of any information it contains.

ARTICLE

Rational design of marigold shape composite Ni₃V₂O₈ flower: a promising catalyst for oxygen evolution reactionRathindranath Biswas^a, Avinava Kundu^a, Monochura Saha^b, Vishaldeep Kaur^c, Biplab Banerjee^a, Rajendra S. Dhayal^a, Ranjit A. Patil^d, Yuan-Ron Ma^d, Tapasi Sen^c, and Krishna Kanta Haldar^{a*}Received 00th January 20xx,
Accepted 00th January 20xx

DOI: 10.1039/x0xx00000x

Advancement of double spinel-type blended metal oxide and designing assorted shaped heterostructured nanomaterials of two different metals in course of action remains a wild zone of research. In this work, we designed marigold flower shaped Ni₃V₂O₈ structure by a basic and effortless thermal decay of Ni(II) 8-hydroxyquinoline and VO(II) 8-hydroxyquinoline molecular precursor using universal and green solvent, water. The marigold flower shaped structure of Ni₃V₂O₈ was characterized using X-ray diffraction (XRD), X-ray photoelectron spectroscopy (XPS), Field-emission scanning electron microscopy (FE-SEM) and Transmission electron microscopy (TEM). Finally, we have tested these marigold flower shaped Ni₃V₂O₈ structure for electrochemical performance, such as Oxygen Evolution Reaction (OER). The results demonstrated that marigold flower shaped Ni₃V₂O₈ structure has superior catalytic activity (overpotential 328 mV at 10 mA cm⁻² and Tafel slope of 61 mV dec⁻¹) compared with physical mixture of V₂O₅ and NiO (overpotential 496 mV at 10 mA cm⁻² and Tafel slope of 158 mV dec⁻¹), pure NiO (overpotential 553 mV at 10 mA cm⁻² and Tafel slope of 205 mV dec⁻¹) or V₂O₅ (overpotential 668 mV at 10 mA cm⁻² and Tafel slope of 314 mV dec⁻¹) in alkaline medium. This higher OER activity of marigold flower shaped Ni₃V₂O₈ structure strengthens its adoption as a potential candidate in the field of energy storage and conversion systems.

1. Introduction

In recent years, the Oxygen Evolution Reaction (OER) carry incredible ramifications for the quest for substitutable energy conversion techniques, for example, water oxidation reactions, rechargeable metal-air batteries¹ and fuel cells² etc. However, the presentation of this electrochemical procedure is restricted by the inherently drowsy kinetics of the OER due to the perplexing four-electron redox procedures, which in turn obstructs the potential application of substitutable energy innovations.^{3, 4} To overcome this inherent kinetics restriction, discovery of an exceptionally dynamic electrocatalyst for OER is urgently required. Be that as it may, the improvement of OER electrocatalyst was found by utilizing RuO₂ and IrO₂, which is not feasible because of their highly expensive nature. Consequently, a huge research exertion has been attempted towards investigating transition metal based electrocatalysts for their potential utilization towards OER. Along these lines, various transition metal based electrocatalysts for example oxides,⁵⁻⁷ hydroxides,⁸⁻¹⁰ sulfides,¹¹⁻¹⁴ selenides,¹⁵⁻¹⁸ phosphides¹⁹⁻²¹ etc. have been widely demonstrated as active

materials for OER. Of late, progress in transition metal oxides, for example MnO₂,^{6, 22} MoO₃,²³ Co₃O₄,^{5, 24} NiO,^{25, 26} Fe₂O₃,²⁷ Fe₃O₄,²⁸ CuO,²⁹ etc. with high activity and ecological kind disposition show noticeable dominance in improving electrochemical exhibitions of OER. Amongst above, either cobalt or nickel-based oxides have been extensively studied because of their enhanced safety, low cost, high chemical and thermal stability.

Hence, low electrical conductivity, huge volume variety and ensuing molecule pummelling upon kinetics limit; make them fairly hard to completely use OER active materials. To address this issue, one appealing methodology is to consolidate the active materials with an electronic substrate, which can improve their electronic conductivity and structure soundness, prompting improved electrochemical execution. Moreover, the electrochemical execution of the readied composite materials displayed a cozy association with the electric substrates. Another procedure is to plan two-fold metal oxides to improve their electrochemical exhibitions. The presentation of the second metal oxides can synergistically improve electrochemical exhibitions in comparison with the single-stage metal oxides, containing synergistic effect, reversible limit and mechanical durability. However, there are various binary spinel-structured mixed metal oxide, for example CuCo₂O₄,³⁰ NiCo₂O₄,^{7, 31, 32} NiFe₂O₄,³³ CoFe₂O₄,³⁴ ZnCo₂O₄,³⁵ CuFe₂O₄,³⁶ MnFe₂O₄,³⁶ MnCo₂O₄^{37, 38} etc. are well documented

^a Department of Chemistry, Central University of Punjab, Bathinda, 151001, India.^b Indian Institute of Science Education and Research Kolkata, Nadia 741246, West Bengal, India^c Institute of Nano Science and Technology, Mohali, 160062, India.^d Department of Physics, National Dong Hwa University, Hualien 97401, Taiwan.

*Electronic Supplementary Information (ESI) available: ATR-FTIR frequency data,

¹H NMR, HRMS, TGA plot, FE-SEM images, EDS, CV, and BET result, etc.

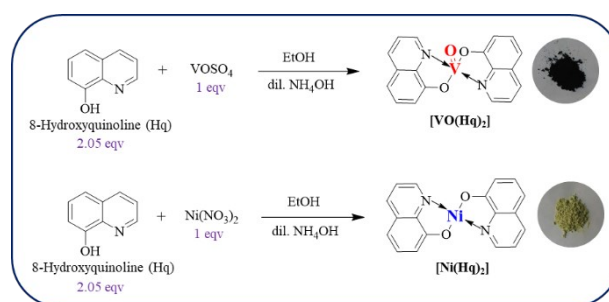
See DOI: 10.1039/x0xx00000x

in literature. Which have indicated preferred electrochemical performance over single-stage metal oxides due to their upgraded electrical and ionic conductivity, reversible limit, and mechanical soundness. Among existing blended oxides, metal vanadates have boundless applications in different fields including photocatalytic water oxidation, oxygen evolution reactions and LIB. Further, these materials are valuable for vitality stockpiling applications since they can offer a lot more extensive potential window starting from the likelihood of the progress metals, particularly, vanadium to exist in an assortment of oxidation states. Vanadium-based blended metal oxides also have a few different focal points for energy capacity, viz. higher energy density, lower cost, and simple accessibility. In addition, the introduction of nickel in the metal vanadates result vanadium-based mixed metal oxides ($\text{Ni}_3\text{V}_2\text{O}_8$) which show astounding electrochemical performance originated from multivalence of nickel and vanadium.

However, synthesis of such binary metal oxides cannot be made directly, as it may be for settled single phase metal oxides nanostructures. Liu et al. have synthesized $\text{M}_3\text{V}_2\text{O}_8$ ($\text{M} = \text{Ni}$ or Co) nanoflake/nanoparticles via chemical co-precipitation technique for high performance pseudocapacitive materials.³⁹ Lv et al. has fabricated $\text{Ni}_3\text{V}_2\text{O}_8$ amorphous wire encapsulated in crystalline tube nanostructure as anode materials for lithium ion batteries by single spinneret electrospinning with subsequent calcination.⁴⁰ Soundharrajan et al. has reported the one-pot synthesis of $\text{Ni}_3\text{V}_2\text{O}_8$ electrodes by a simple metal organic framework-combustion technique for anode applications in Li-ion batteries.⁴¹ Sambandam et al. has synthesised $\text{Ni}_3\text{V}_2\text{O}_8$ nanoparticles as an excellent anode material for high-energy lithium-ion batteries through a zeoliticimidazolate framework intermediate precipitation method using water as a solvent.⁴² Liu et al. has synthesised $\text{Ni}_3\text{V}_2\text{O}_8$ sensing electrode for ammonia (NH_3) detection by sol-gel method.⁴³ Wang et al. has reported an efficient two-step hydrothermal synthesis method to synthesize $\text{Ni}_3\text{V}_2\text{O}_8$ nanowires arrays organized by ultrathin nanosheets for enhanced lithium storage properties.⁴⁴ Briefing the results from the literature, it has been observed that $\text{Ni}_3\text{V}_2\text{O}_8$ mixed oxide structures were mostly synthesized by multiple steps technique. To the best of our knowledge, there is no report till date on the preparation of marigold flower shaped $\text{Ni}_3\text{V}_2\text{O}_8$ structure in one pot utilizing Ni(II) 8-hydroxyquinoline and VO(II) 8-hydroxyquinoline complex atomic forerunner via a hydrothermal process. Herein, we fabricated marigold flower shaped $\text{Ni}_3\text{V}_2\text{O}_8$ structure by a simple and facile thermal decomposition of Ni(II) 8-hydroxyquinoline $[\text{Ni}(\text{Hq})_2]$ and VO(II) 8-hydroxyquinoline $[\text{VO}(\text{Hq})_2]$ complexes in presence of a universal solvent, water. Finally, we have explored these Marigold flower shaped $\text{Ni}_3\text{V}_2\text{O}_8$ for OER and exhibit magnificent OER activity compared to its constituent oxide as the potential electrode materials.

2. Result and discussion

The $[\text{Ni}(\text{Hq})_2]$ and $[\text{VO}(\text{Hq})_2]$ complexes were synthesized by previously reported procedure with small tuning (Scheme 1). The synthesized compounds were characterized by various spectroscopic technique such as ^1H NMR, ^{13}C NMR, ATR-FTIR, and also with high-resolution mass spectrometry. Various characterization techniques such as FE-SEM, HRTEM, SEAD, power XRD, XPS, TGA, etc. are utilization to explore the growth of Marigold flower shaped $\text{Ni}_3\text{V}_2\text{O}_8$ structure. Finally, we have employed these marigold flower shape $\text{Ni}_3\text{V}_2\text{O}_8$ structure based composite oxide as electrocatalyst active materials for Oxygen Evolution Reaction. Surprisingly, these marigold flower shaped $\text{Ni}_3\text{V}_2\text{O}_8$ structure based composite displays superior OER activity compared to commercial IrO_2 and remarkable cycle strength. The as-fabricated marigold flower shaped $\text{Ni}_3\text{V}_2\text{O}_8$ structure are cheap yet profoundly proficient OER electrocatalyst.



Scheme 1. Synthesis of $\text{VO}(\text{Hq})_2$ and $\text{Ni}(\text{Hq})_2$ complexes using dil. NH_4OH (2M), EtOH, pH= 6.5-7.0 at room temperature.

2.1. Spectroscopic analysis

As the ligand and both $[\text{Ni}(\text{Hq})_2]$ and $[\text{VO}(\text{Hq})_2]$ complexes show the distinct characteristic absorption property, the UV-Vis spectroscopy were used to identify complexation and understanding the coordinational behaviours of Ni^{2+} and VO^{2+} metal ions with Hq ligands. The UV-Vis spectra of ligands and both $[\text{Ni}(\text{Hq})_2]$ and $[\text{VO}(\text{Hq})_2]$ complexes were recorded at room temperature in chloroform solvent. Both the complex formation was monitored by spectral changes during the UV-Vis measurements were shown in Fig. 1. The absorbance peaks appeared at 241 and 314 nm (Fig. 1a) corresponds to intra-ligands $\pi-\pi^*$ transition of 8-hydroxyquinoline(Hq). However, in case of $[\text{Ni}(\text{Hq})_2]$ complex (Fig. 1b), this intra-ligands $\pi-\pi^*$ type transition was shifted bathochromically from 241 and 314 nm to 284 and 345 nm, respectively and resulting the formation of due $[\text{Ni}(\text{Hq})_2]$ complex. Notably, a new broad peak at 405 nm was observed in the UV-Vis spectrum of $[\text{Ni}(\text{Hq})_2]$ and this can be attributed by assigning the mixed absorption modes caused by intra-ligand transitions and Ni^{2+} to Hq ligands charge transfer which is consistent with the previously reported result⁴⁵⁻⁴⁷. On the other hand, $[\text{VO}(\text{Hq})_2]$ complex in the chloroform solution shows almost similar absorbance spectra to that of $[\text{Ni}(\text{Hq})_2]$ complex where the absorbation maxima at 241 and 314 nm were shifted bathochromically to the λ_{max} 250 and 390 nm, respectively (Fig. 1c). It has been reported that absorbance band appeared in

the range of 450-600 nm can be attributed to the ligands to metal charge transfer transitions where the transitions were most likely due to involving ligands orbital only.^{22, 48-50}

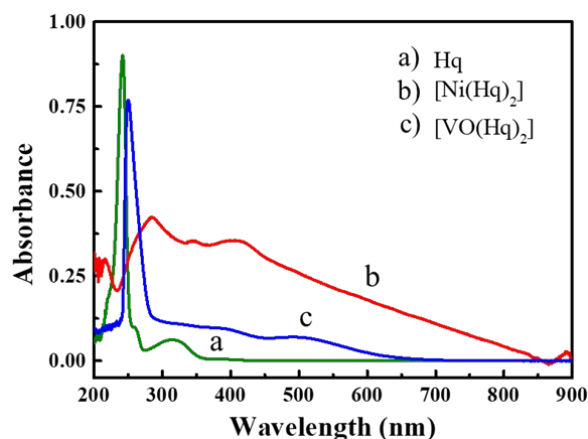


Fig. 1 UV-vis spectrum of (a) Hq, (b) $[\text{Ni}(\text{Hq})_2]$ and (c) $[\text{VO}(\text{Hq})_2]$ complexes in chloroform at room temperature.

To further know the formation of $[\text{Ni}(\text{Hq})_2]$ and $[\text{VO}(\text{Hq})_2]$ complexes, we have studied ATR-FTIR spectroscopy. Formation of $[\text{Ni}(\text{Hq})_2]$ was affirmed by the characteristic peaks at 297 and 278 cm^{-1} corresponding to asymmetric and symmetric stretching mode of Ni-O bond along with asymmetric and symmetric stretching mode of Ni-N bond appeared at 258 and 231 cm^{-1} , respectively (Fig. 2a).^{51, 52} In Fig. 2b the strong peak centred at 950 cm^{-1} due to V=O stretching.^{53, 54} This low stretching frequency imply substantial weakening of the V=O bond, consistent with strong σ and π electron donation by 8-hydroxyquinoline to antibonding orbitals of the V=O group. Where the bands appeared at 373, 347 and 301 cm^{-1} are attributed to V-O stretching modes and the peaks at 258 and 233 cm^{-1} are assigned to V-N stretching modes^{51, 55}, which confirm the formation of $[\text{VO}(\text{Hq})_2]$ complex (details ATR-FTIR stretching modes are given in Table S1).

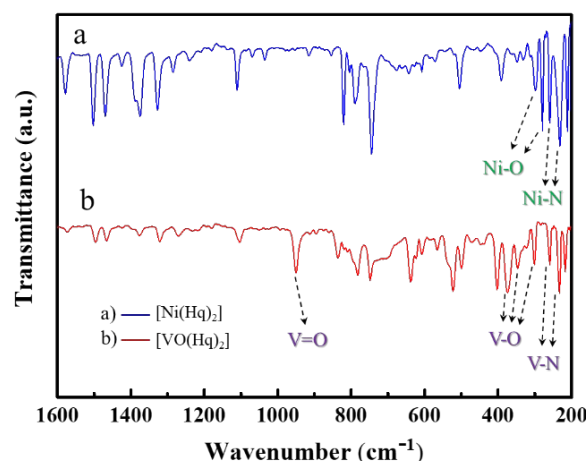


Fig. 2 ATR-FTIR spectra of (a) $[\text{Ni}(\text{Hq})_2]$ and (b) $[\text{VO}(\text{Hq})_2]$ complexes.

Finally, $[\text{Ni}(\text{Hq})_2]$ and $[\text{VO}(\text{Hq})_2]$ complexes were confirmed by ^1H NMR, ^{13}C NMR and High resolution mass spectroscopy. The ^1H NMR spectra of free Hq shows well intense signal within range 7.2 ppm to 8.7 ppm^{56, 57}. The ^1H NMR of $[\text{Ni}(\text{Hq})_2]$ reveal broadened and shifted signals to high frequencies (Fig. S1) and confirmed the presence and coordination of Hq with Ni(II) centre. Additionally, the ESI-MS (Positive mode) spectra (Fig. S2 and S3) shows the most intense peak at m/z 347.0313 (Calcd 347.0331) corresponding to molecular weight of $[\text{Ni}(\text{Hq})_2]$, which is assumed to be a species with a 1:2 (metal to ligand) stoichiometry. Similarly, the ^1H NMR spectra of $[\text{VO}(\text{Hq})_2]$ was to assign to Hq signals to coordination with V(IV) metal (Fig. S4). Further, the mass spectra show peak at m/z 356.0314 (356.0366) and cumulatively both spectra confirmed the molecular formula of $[\text{VO}(\text{Hq})_2]$ (Fig. S5).

To study the thermal stability of $[\text{Ni}(\text{Hq})_2]$ and $[\text{VO}(\text{Hq})_2]$ complexes and understand the fabrication of marigold shape $\text{Ni}_3\text{V}_2\text{O}_8$ flower, we have performed the Thermogravimetric analysis (TGA) of $[\text{Ni}(\text{Hq})_2]$ and $[\text{VO}(\text{Hq})_2]$ complexes. Fig. S6 represents the TGA curve of $[\text{Ni}(\text{Hq})_2]$ and $[\text{VO}(\text{Hq})_2]$ complexes. The thermogram (Fig. S6a) of $[\text{Ni}(\text{Hq})_2]$ complex exhibits two distinct cut stages. The first step shows the initial 11% weight loss in the temperature range of 100-170 $^\circ\text{C}$ where in the second stage 71% weight loss is observed in the temperature range of 180-450 $^\circ\text{C}$. Thermal decomposition of the $[\text{VO}(\text{Hq})_2]$ complex occurs in multiple stages (Fig. S6b). No sharp weight change is observed. The thermogram of $[\text{VO}(\text{Hq})_2]$ complex shows 7% weight loss by two stage decomposition stage in the temperature range 35-285 $^\circ\text{C}$, where 70% weight loss is observed in the temperature range 290-558 $^\circ\text{C}$ by multiple stage decomposition. A further increase in temperature above 450 $^\circ\text{C}$ (490 $^\circ\text{C}$ for $[\text{VO}(\text{Hq})_2]$ complex) reveals no loss in weight and this constant weight is due to nickel oxide or vanadium oxide (confirmed by XRD studies), which appears as a final pyrolysis product of $[\text{Ni}(\text{Hq})_2]$ and $[\text{VO}(\text{Hq})_2]$ complexes.

2.2 Morphology Investigation

Architecture of marigold flower shaped $\text{Ni}_3\text{V}_2\text{O}_8$ structure was optimised after performing a number of controlled reactions to changing several reaction parameters, for example, reaction time, variation of precursor concentration ratios, growth temperature etc. It was indicated in the experimental section that the marigold flower shaped $\text{Ni}_3\text{V}_2\text{O}_8$ structure were fabricated by mixing $[\text{Ni}(\text{Hq})_2]$ and $[\text{VO}(\text{Hq})_2]$ complexes in 3:2 molar ratio under hydrothermal methods in one pot. We have also conducted the same reaction under identical conditions in absence of $[\text{VO}(\text{Hq})_2]$ complexes and got anisotropic NiO micro rod shape structure (Fig. S7a-b). On the other hand, without $[\text{Ni}(\text{Hq})_2]$ complexes, the same reaction produced V_2O_5 structure having mixture of spheres and rods shape (Fig. S7c-d) and the corresponding energy dispersive x-ray spectroscopy (EDS) of V_2O_5 and NiO micro rods are shown in the Fig. S8.

We have tested the similar reaction under the same conditions at different time intervals (like 8, 16 and 24h) but didn't produce desired shape of $\text{Ni}_3\text{V}_2\text{O}_8$ structure (Fig. S9a-c). No products were found at temperature below 190°C , even the hydrothermal reaction continued for 72h (Fig. S9d). Therefore, the use of a molar ratio 3:2 of $[\text{Ni}(\text{Hq})_2]$ and $[\text{VO}(\text{Hq})_2]$ complexes is critical to achieve marigold flower shaped $\text{Ni}_3\text{V}_2\text{O}_8$ structure.

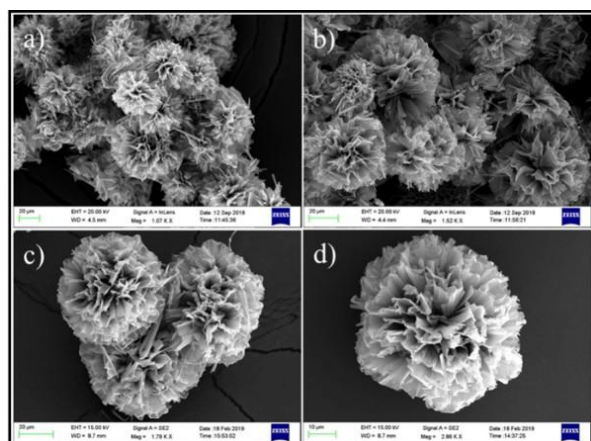


Fig. 3 FE-SEM images of marigold shape $\text{Ni}_3\text{V}_2\text{O}_8$ flower: (a), (b) and (c) panoramic FE-SEM images and (d) FE-SEM image of a single $\text{Ni}_3\text{V}_2\text{O}_8$ flower

The morphology of $\text{Ni}_3\text{V}_2\text{O}_8$ structure was observed using field emission SEM equipped with EDS and high resolution TEM. Fig. 3a-d shows representative panoramic FE-SEM images of $\text{Ni}_3\text{V}_2\text{O}_8$ structures. The FE-SEM images clearly reveal the formation of marigold flower like $\text{Ni}_3\text{V}_2\text{O}_8$ structures with diameter of $66 \pm 3 \mu\text{m}$.

These marigold flower shaped $\text{Ni}_3\text{V}_2\text{O}_8$ structures were further investigated by TEM to get detailed structural information. TEM images shown in Fig. 4a-c clearly illustrate the fabrication of flowers-shaped structure having a sheet-like within the flower. The sheet thickness of the $\text{Ni}_3\text{V}_2\text{O}_8$ flower was around $\sim 7.5 \pm 3 \text{ nm}$ (Fig. 4b). The presence of clear lattice fringes showing the (131) planes in the inset images (Fig. 4cⁱ) in high resolution TEM (HRTEM) indicates that the individual nanosheets are single crystalline in nature as shown in Fig. 4c.

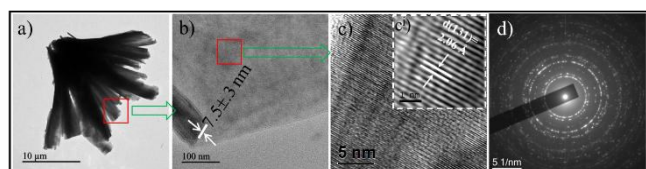


Fig. 4 TEM images of marigold shape $\text{Ni}_3\text{V}_2\text{O}_8$ flower at different magnifications, (a) TEM image where area is marked to achieve the HRTEM. The inset (cⁱ) is the lattice spaces obtaining from HRTEM image of (b) showing the (131) planes of the $\text{Ni}_3\text{V}_2\text{O}_8$ flower, (d) Represents the typical SAED pattern of $\text{Ni}_3\text{V}_2\text{O}_8$ flower.

However, the $\text{Ni}_3\text{V}_2\text{O}_8$ flower in whole is polycrystalline in nature as indicated by SAED pattern shown in inset of Fig. 4d. Both of high magnification FE-SEM image and the TEM image clearly shows that the curly and folded thin nanosheets of thickness of $7.5 \pm .3 \text{ nm}$ are branched out from the central zone of the flower. These marigold shape $\text{Ni}_3\text{V}_2\text{O}_8$ structures were further analysed to get detailed compositional information by elemental mapping as shown in Fig. 5.

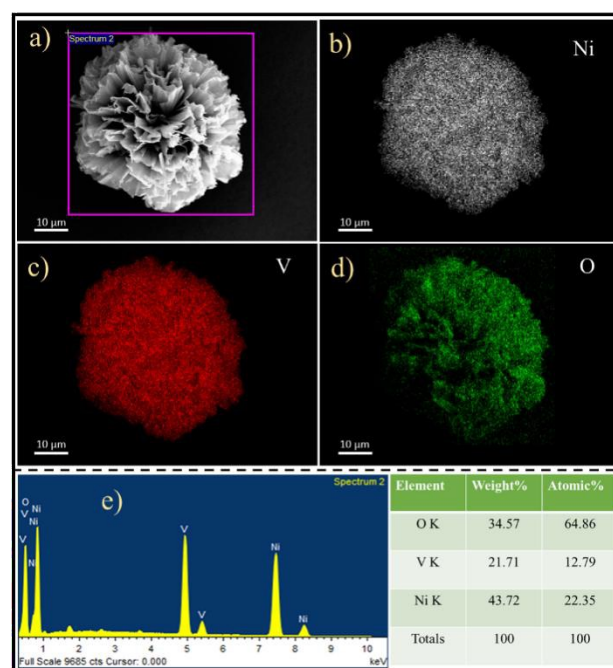


Fig. 5 (a) FE-SEM image of marigold shape $\text{Ni}_3\text{V}_2\text{O}_8$ flower and corresponding elemental mapping: (b) Ni, (c) V, (d) O of marigold shape $\text{Ni}_3\text{V}_2\text{O}_8$ flower and (e) EDS of marigold shape $\text{Ni}_3\text{V}_2\text{O}_8$ flower.

The elemental mapping study clearly revealed that Ni, V and O are the fundamental elements exist (Fig. 5b-d) in $\text{Ni}_3\text{V}_2\text{O}_8$ flower and it was also observed that Ni, V and O elements are well-dispersed throughout $\text{Ni}_3\text{V}_2\text{O}_8$ flower. The EDS (Fig. 5e) data show no other contaminations were detected in the $\text{Ni}_3\text{V}_2\text{O}_8$ flower.

2.3. Structural Analysis

With the aim of getting of crystalline structures and identify the crystal phases of $\text{Ni}_3\text{V}_2\text{O}_8$ flowers and pure V_2O_5 and NiO structures, we have analyzed the powder X-ray diffraction (XRD) study. Fig. 6a shows the XRD pattern of as synthesized V_2O_5 micro rods. The narrow and intense diffraction peaks centered at $2\theta = 15.4^\circ, 20.3^\circ, 21.7^\circ, 26.1^\circ, 31.1^\circ, 32.4^\circ, 34.3^\circ, 41.3^\circ, 42.0^\circ, 45.4^\circ, 47.3^\circ, 48.8^\circ, 51.2^\circ, 52.0^\circ, 55.6^\circ, 61.1^\circ$ and 62.1° corresponded to (020), (001), (011), (110), (040), (101), (130), (002), (012), (141), (060), (102), (200), (061), (201), (240), and (170) planes, respectively indicate that V_2O_5 structures (JCPDS No. 60-0767) were highly crystalline.⁵⁸ No diffraction peak for other contaminations was detected, indicating the high purity of as synthesized V_2O_5 structure. Fig. 6b presents the XRD pattern of as synthesized NiO

nanostructures. Peaks appeared at $2\theta = 36.98^\circ$ (110), 43.0° (200), 62.6° (220), 75.1° (311) and 79.1° (222) are attributed to cubic NiO (PDF 01-078-4359) and clearly conform the formation of crystalline NiO nanostructures.^{59, 60} Fig. 6c shows the XRD pattern of as synthesized marigold shape $\text{Ni}_3\text{V}_2\text{O}_8$ flowers. The strong peaks appeared at $2\theta = 35.8^\circ$ (122), 43.2° (151), and 62.8° (442) along with weak peaks at 18.9° (120), 31.2° (131), 58.5° (162) conform the formation of $\text{Ni}_3\text{V}_2\text{O}_8$ structures (PDF 01-074-1485). Additionally, EDS analysis justifies the presence of the elements Ni, V, and O in the $\text{Ni}_3\text{V}_2\text{O}_8$ flowers as shown in Fig. 5e. EDS study also reveals that there are no other impurities as well Ni, V and O elements and supports the XRD analysis of $\text{Ni}_3\text{V}_2\text{O}_8$ structures.

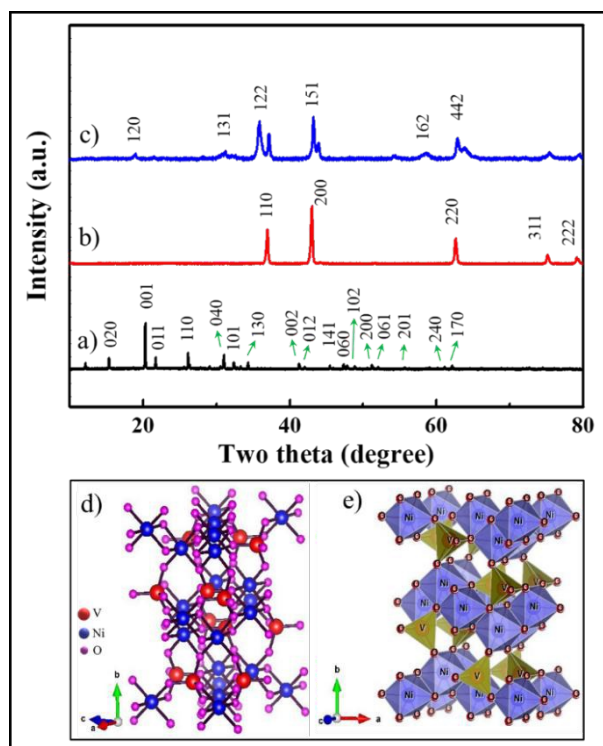


Fig. 6 Upper panel: XRD pattern of as synthesized (a) V_2O_5 micro rods, (b) NiO micro rods, and (c) Marigold shape $\text{Ni}_3\text{V}_2\text{O}_8$ flowers. Lower panel: (e) and (d) display a coordinating octahedron representation of crystal structure of $\text{Ni}_3\text{V}_2\text{O}_8$.

The majority of the diffraction peaks were all around recorded to the standard orthorhombic crystal system of $\text{Ni}_3\text{V}_2\text{O}_8$ (JCPDS No. 074-1484) having a place with the Acam space group with unit cell parameters a , b , and c determined to be 8.2400, 11.3800, and 5.9060 Å individually. In this spinel Ni^{2+} ions structure an edge shared NiO_6 (octahedral) layers, which are isolated by VO_4 (V^{5+} ions, tetrahedral), bringing about a curious Kagome'- staircase geometry.⁶¹

To further confirm the chemical composition and electronic structure, for example valence state, of each element in the $\text{Ni}_3\text{V}_2\text{O}_8$ flowers, XPS investigation was performed and the corresponding results are revealed in Fig. 7. The survey scan of the $\text{Ni}_3\text{V}_2\text{O}_8$ flowers presented in Fig. 7a, suggests the presence

of Ni, V, and O and the nonappearance of other contamination. The C peak arises from the reference. The high-resolution scan for Ni 2p is shown in Fig. 7b. There are two major peaks at 873.4 and 855.7 eV, which are assigned to the Ni $2p_{1/2}$ and $2p_{3/2}$ spin-orbit peaks of $\text{Ni}_3\text{V}_2\text{O}_8$, respectively. In addition, "shake up" satellite peaks of Ni 2p are also observed at the binding energies 879.5 and 861.6 eV.^{40, 62} The deconvoluted Ni $2p_{3/2}$ spectrum into two distinct peaks at the binding energy of 855.5 and 856.7 eV, indicating the occurrence of both Ni (II) and Ni (III) state in $\text{Ni}_3\text{V}_2\text{O}_8$ flower.⁶³ It has been reported that both V (IV) and V (V) state may be observed in some vanadates, with heavily close binding energy of 516.4-517.4 eV (V^{5+} , $2p_{3/2}$) and 515.4-515.75 eV (V^{4+} , $2p_{3/2}$).^{64, 65} Thus, the peaks fitted in the XPS spectrum of V 2p area at binding energies of 517.17 eV and 515.62 eV can be ascribed to $\text{V}^{5+} 2p_{3/2}$ and $\text{V}^{4+} 2p_{3/2}$, respectively (Fig. 7c).

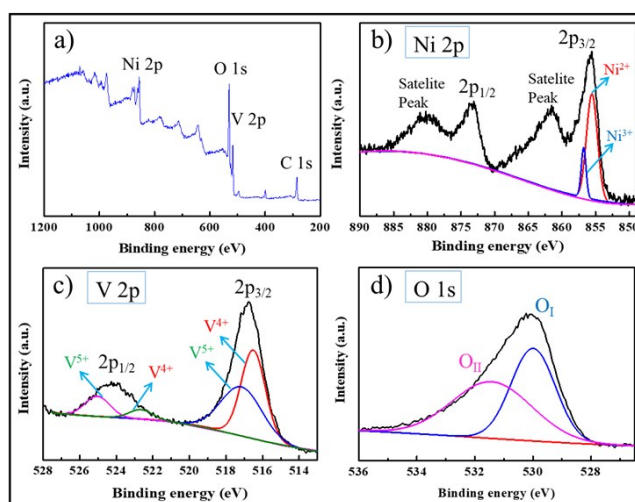


Fig. 7 XPS spectra: (a) survey spectra, (b) Ni 2p, (c) V 2p, (d) O 1s in as-synthesized marigold shape $\text{Ni}_3\text{V}_2\text{O}_8$ flowers.

Therefore, the coupling of $\text{Ni}^{3+}/\text{Ni}^{2+}$ and $\text{V}^{5+}/\text{V}^{4+}$ can be confirmed in the as-synthesized $\text{Ni}_3\text{V}_2\text{O}_8$ flowers, and the interaction between these mixed valences ions may attribute to the improvement of the overall electrochemical performance. There appear two types of oxygen (O^{2-}) ions in O XPS profile (denoted as O^I and O^{II}) (Fig. 7d). The O^I ions at 530.8 eV corresponds to lattice oxygen atoms which are in a fully-coordinated environment, and the other O^{II} ions at 532.8 eV are O^{2-} , suggesting the oxygen-deficient regions within the $\text{Ni}_3\text{V}_2\text{O}_8$ phase.

3. Electrochemical Studies (OER Activity)

Apart from the morphology and composition study, the electrochemical OER activity of the as synthesised Marigold flower shaped $\text{Ni}_3\text{V}_2\text{O}_8$ samples was compared with physical mixture of V_2O_5 and NiO, pure NiO and V_2O_5 , using linear sweep voltammetry (LSV) technique measurements performed in 1 M KOH solution. In correlation, commercial IrO_2 was picked as reference. Fig. 8a depicts the LSV curves of $\text{Ni}_3\text{V}_2\text{O}_8$, physical mixture of V_2O_5 and NiO, pure NiO and V_2O_5 catalysts.

Marigold flower shaped $\text{Ni}_3\text{V}_2\text{O}_8$ achieved the current density of 10 mA cm^{-2} at an overpotential of only 328 mV whereas commercial IrO_2 shows similar current density at an overpotential of 360 mV. Similarly, $\text{Ni}_3\text{V}_2\text{O}_8$ shows premier OER activity over the physical mixture of V_2O_5 and NiO, pure NiO and V_2O_5 for attaining current density of 10 mA cm^{-2} at overpotential of 496, 553 and 668 mV, respectively. In order to figure out the kinetics of OER processes, Tafel polarization plot is an important tool that can be used to determine the mechanistic pathway of the OER activity. From the linear fitting of the Tafel plot, the Tafel slope derived from the corresponding LSV curves were shown in Fig. 8b and was found to be 61 mV dec^{-1} for $\text{Ni}_3\text{V}_2\text{O}_8$ flower composite structure, which is much lesser than that of physical mixture of V_2O_5 and NiO, (158 mV dec^{-1}) and its constituent NiO (205 mV dec^{-1}) and V_2O_5 (314 mV dec^{-1}) catalyst. Notably, $\text{Ni}_3\text{V}_2\text{O}_8$ flower exhibits lower Tafel slope than commercial IrO_2 (65 mV dec^{-1}). These observations also underpin the superior OER activity of the Marigold shape $\text{Ni}_3\text{V}_2\text{O}_8$ flower catalyst.

analysis and suggests that Marigold flower shaped $\text{Ni}_3\text{V}_2\text{O}_8$ displays the quickest charge-transfer process among all the three electrocatalyst, which might be due to the rough surface of the catalyst resulting in the extraordinary OER activity. Thus, this Marigold flower shaped $\text{Ni}_3\text{V}_2\text{O}_8$ flower 3D structures improve the overall surface area reasonable for better catalysis. Hence, to study the relationship between the catalytic activities and the surface accessibility of $\text{Ni}_3\text{V}_2\text{O}_8$ flower along with physical mixture of V_2O_5 and NiO, pure NiO and V_2O_5 catalyst, the electrochemically active surface area (ECSA) was measured in terms of double layer capacitance (C_{dl}). Both the anodic and cathodic double-layer charging currents (J_a and J_c , respectively) were measured from the CV curves (Fig. 9a) at a fixed potential of 0.2 V and are plotted against corresponding scan rates (Fig. 9b). The calculated C_{dl} for $\text{Ni}_3\text{V}_2\text{O}_8$ flower is 2.72 mF cm^{-2} and the corresponding ECSA is found to be 68 cm^2 , which remained much higher than that of physical mixture of V_2O_5 and NiO or pure NiO and V_2O_5 catalyst (Fig. S10) (details are summarized in Table 1).

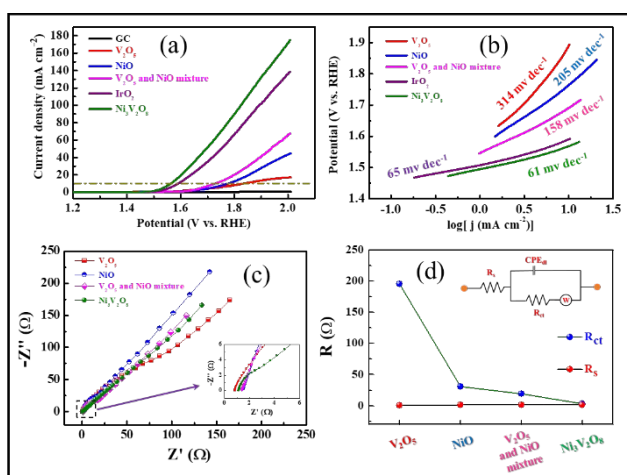


Fig. 8 The parameters of evaluating the catalytic performance: (a) polarization curves (LSV) plot and (b) corresponding Tafel plots of IrO_2 , $\text{Ni}_3\text{V}_2\text{O}_8$, physical mixture of V_2O_5 and NiO, NiO and V_2O_5 catalyst, (c) electrochemical impedance spectra at 350 mV (Ag/AgCl), and (d) variation of R_s and R_{ct} of $\text{Ni}_3\text{V}_2\text{O}_8$, physical mixture of V_2O_5 and NiO, NiO and V_2O_5 catalyst.

To further get insight into the superior catalytic activity of Marigold shape $\text{Ni}_3\text{V}_2\text{O}_8$ flower, electrochemical impedance spectroscopy (EIS) was studied and displayed in Fig. 8c. From the EIS analysis, it has been found that $\text{Ni}_3\text{V}_2\text{O}_8$ flower exhibits lowest charge transfer resistance (R_{ct}) of 3.4Ω , whereas physical mixture of V_2O_5 and NiO, pure NiO and V_2O_5 possess R_{ct} of 19.2Ω , 23.9Ω and 195.1Ω , respectively (Table 1). The solution resistance (R_s) of $\text{Ni}_3\text{V}_2\text{O}_8$, physical mixture of V_2O_5 and NiO, NiO, and V_2O_5 was found to be 1.11 , 1.38 , 1.5 , and 0.82Ω , respectively (Table 1). The lowest R_{ct} value of $\text{Ni}_3\text{V}_2\text{O}_8$ indicates that Marigold flower shaped $\text{Ni}_3\text{V}_2\text{O}_8$ is electrocatalytically more active towards OER compared to physical mixture of V_2O_5 and NiO, pure NiO and V_2O_5 catalyst. This impedance result is in good agreement with the LSV

Table 1. Comparative results of OER performance of IrO_2 , physical mixture of V_2O_5 and NiO, V_2O_5 , NiO, and $\text{Ni}_3\text{V}_2\text{O}_8$ catalysts.

System	Overpotential at 10 mA cm^{-2}	Tafel slope (mV dec^{-1})	R_{ct} (Ω)	R_s (Ω)	C_{dl} (mF cm^{-2})	ECSA (cm^2)	Surface area ($\text{m}^2 \text{g}^{-1}$)
V_2O_5	668 mV	314	195.1	0.82	0.2095	5.23	4.543
NiO	553 mV	205	23.9	1.5	0.422	10.55	8.642
V_2O_5 and NiO mixture	496 mV	158	19.2	1.38	0.565	14.12	-
IrO_2	360 mV	65	-	-	-	-	-
$\text{Ni}_3\text{V}_2\text{O}_8$	328 mV	61	3.4	1.11	2.72	68	11.47

Further, the Brunauer-Emmett-Teller (BET) estimation results proved this pattern, where the $\text{Ni}_3\text{V}_2\text{O}_8$ flower has the largest surface area of $11.47 \text{ m}^2 \text{ g}^{-1}$, trailed by NiO ($8.642 \text{ m}^2 \text{ g}^{-1}$) and V_2O_5 ($4.543 \text{ m}^2 \text{ g}^{-1}$) (Fig. S11). Again, the LSV curves of $\text{Ni}_3\text{V}_2\text{O}_8$ flower, physical mixture of V_2O_5 and NiO, NiO, and V_2O_5 electrodes were normalized to explain the OER activity. As presented in Fig. S12, the $\text{Ni}_3\text{V}_2\text{O}_8$ flower electrodes exhibit superior OER activity (current standardized by ECSA) compared to its constituent oxide due to higher specific OER activity of $\text{Ni}_3\text{V}_2\text{O}_8$ flower electrodes. The specific OER correlation affirms that the formation of $\text{Ni}_3\text{V}_2\text{O}_8$ spinel flower results in larger intrinsic activity.

Catalytic durability is another important parameter for an efficient electrocatalyst. Here, we examined the long-term 2000 continuous LSV cycles using 1M KOH solution an electrolyte. Fig. 9c shows the LSV curve of initial and after 2000th cycle of $\text{Ni}_3\text{V}_2\text{O}_8$ electrode. After 2000 LSV cycles, the change in the overpotential at current density of 10 mA cm^{-2} was found to be only 8 mV (from 328 mV to 336 mV) which demonstrates the long-term superior stability of the $\text{Ni}_3\text{V}_2\text{O}_8$ flower toward OER activity.

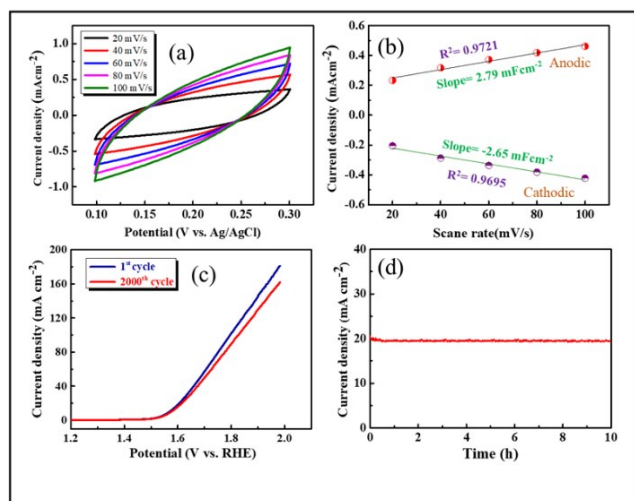
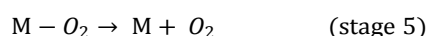
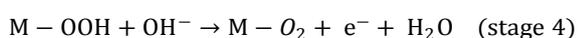
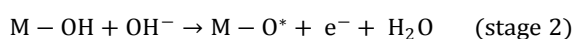
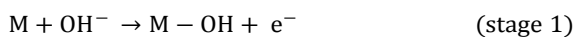


Fig. 9 (a) Cyclic voltammograms of $\text{Ni}_3\text{V}_2\text{O}_8$, (b) plot of J_a and J_c against scan rate for the determination of double layer capacitance (C_{dl}). Stability test: (c) Polarization curves of the $\text{Ni}_3\text{V}_2\text{O}_8$ after 1st and 2,000th cycles of continuous operation and (d) Chronoamperometric study of $\text{Ni}_3\text{V}_2\text{O}_8$ at an overpotential of 369 mV for 10 h.

Further, we have also checked the stability of the $\text{Ni}_3\text{V}_2\text{O}_8$ catalyst by chronoamperometric method and found a current density of 20 mA cm^{-2} for 10 hours constantly (Fig. 9d). Thus, overall electrochemical observations conclude that $\text{Ni}_3\text{V}_2\text{O}_8$ flowers are promising catalyst for the OER activity in alkaline medium. And from OER investigations, we believe that nickel oxide unit in $\text{Ni}_3\text{V}_2\text{O}_8$ as a catalyst precursor and vanadium oxide in the $\text{Ni}_3\text{V}_2\text{O}_8$ flowers serve as the actual reactant site to produce oxygen with the persistent activation of the catalyst.

3.1 OER Pathway

The overall OER pathways under basic condition start with the adsorption and release of the OH^- anion at the catalyst surface of a functioning metal site (M) to make adsorbed OH^- species (stage 1). The adsorbed OH species further react with OH^- to generate H_2O and adsorbed atomic O^* and discharge an electron (stage 2). After that, an OH^- anion reacts with an adsorbed O^* atom to produce adsorbed OOH (stage 3). Moreover, further reaction with extra OH^- anions generates adsorbed O_2 and H_2O (stage 4). Adsorbed O_2 then discharge in the stage 5. All the steps associated in the reaction mechanism have been portrayed as follows:^{7, 66, 67}



The electrocatalytic OER activity of $\text{Ni}_3\text{V}_2\text{O}_8$, physical mixture of V_2O_5 and NiO , pure NiO , and V_2O_5 materials belongs to heterogeneous catalytic reaction where the M–O interaction within the intermediates of MOH, MO and MOOH are very essential for the general electrocatalytic performance of the catalysts. The high OER activity of $\text{Ni}_3\text{V}_2\text{O}_8$ can be attributed to the synergetic effect between variable oxidation state of V (V^{5+} and V^{4+}) and Ni (Ni^{3+} and Ni^{2+}) metal ions which provide more active metal site for the adsorption of the OH^- anion (stage 1) on the surface of $\text{Ni}_3\text{V}_2\text{O}_8$ and consequently facilitates the other steps for OER. Therefore, it can be concluded that as Marigold shape $\text{Ni}_3\text{V}_2\text{O}_8$ flower possesses highest electrochemical active surface area and active metal sites over physical mixture of V_2O_5 and NiO , pure NiO , and V_2O_5 catalyst, hence $\text{Ni}_3\text{V}_2\text{O}_8$ exhibits highest OER activity in alkaline medium.

4. Experimental Section

4.1 Materials

Vanadyl sulphate ($\text{VOSO}_4 \cdot 5\text{H}_2\text{O}$, 95%, Molychem, AR), nickel nitrate hexahydrate ($[\text{Ni}(\text{NO}_3)_2 \cdot 6\text{H}_2\text{O}]$ (Loba Chemie), 8-hydroxyquinoline (Loba Chemie, AR/ACS 99%), ammonium hydroxide solution (NH_4OH , 25%, AR), ethanol (AR), chloroform (Loba Chemie), potassium hydroxide (KOH, Loba Chemie), Iridium oxide (IrO_2 , Sigma-Aldrich), 5% Nafion™ 117 solution (Sigma-Aldrich). The chemicals used in this work were of analytical grade and utilized directly after purchase without further purification. Double distilled water (DDW) (18.2 millipores) was used in all respect.

4.2 Synthesis of Ni(II) 8-Hydroxyquinoline Complex $[\text{Ni}(\text{Hq})_2]$

$[\text{Ni}(\text{Hq})_2]$ was synthesised here by adopting a reported method with little modification,⁶⁸ In a typical synthesis procedure, 1.5 mmol (436.20 mg) of $\text{Ni}(\text{NO}_3)_2$ was dissolved in 10 mL ethanol. 3.075 mmol (446.43 mg) of 8-Hydroxyquinoline was dissolved in 30 mL ethanol in a 100 mL round bottom flask. Separate solution of $\text{Ni}(\text{NO}_3)_2$ and 8-hydroxyquinoline were prepared in a 1: 2.05 molar ratio. Then the $\text{Ni}(\text{NO}_3)_2$ solution was added drop wise into the solution of 8-hydroxyquinoline under stirring condition at room temperature (Scheme I). The pH of each solution was adjusted to 6.5–7.0 by adding 2M NH_4OH solution. The reaction was continued for 150 minutes. Thereafter the reaction mixture was filtered out and yellow-green precipitate was collected, washed with DDW followed by ethanol to remove excess 8-hydroxyquinoline for several times, and dried at 90°C .

^1H NMR and TOF-MS of $[\text{Ni}(\text{Hq})_2]$ Complex

^1H NMR ($\text{DMSO}-d_6$) δ 15.30 (b, 1H), 17.02 (b, 1H), 18.30 (b, 2H), 20.49 (b, 2H) (Fig. S1). TOF-MS: m/z $[\text{M}+\text{H}]^+$ calculated for $\text{C}_{18}\text{H}_{13}\text{N}_2\text{O}_2\text{Ni}$ is 347.0331, found 347.0313 (Fig. S2) and calc. for $\text{C}_{18}\text{H}_{12}\text{N}_2\text{O}_2\text{NiNa}$ $[\text{M}+\text{Na}]^+$ is 360.0150 found 369.0068 (Fig. S3).

4.3 Synthesis of VO(II) 8-Hydroxyquinoline Complex [VO(Hq)₂]

[VO(Hq)₂] was synthesised by the same methods as Ni(II) 8-Hydroxyquinoline complex was synthesised. 1.5 mmol (379.62 mg) of VOSO₄ was dissolved in a solution of 10 mL ethanol and 15 mL double distilled water. 3.075 mmol (446.43 mg) of 8-Hydroxyquinoline was dissolved in 30 mL ethanol in a 100 mL round bottom flask. Separate solution of VOSO₄ and 8-Hydroxyquinoline were prepared in a 1: 2.05 molar ratio. Then the VOSO₄ solution was added drop wise in to the solution of 8-Hydroxyquinoline under stirring condition at room temperature. The pH of each solution was adjusted to 6.5-7.0 by adding 2M NH₄OH solution. The reaction was continued for 150 minutes. Thereafter the reaction mixture was filtered out and yellow-green precipitate was collected, washed with DDW followed by ethanol to remove excess 8-Hydroxyquinoline for several times, and dried at 90°C.

¹H NMR and TOF-MS of [VO(Hq)₂] Complex

¹H NMR (400 MHz, MeOH-*d*₄) δ 7.14 (d, 2H, 7.96), 7.27 (d, 2H, J = 5.68), 7.58 (mt, 2H), 7.33 (d, 6.4 Hz), 8.17 (d, 1H, J = 4.4 Hz), 8.27 (d, 1H, J = 6.4 Hz), 8.35 (d, 1H, J = 2.92 Hz), 8.56 (d, 1H, J = 3.2 Hz) (Fig. S4). TOFMS: *m/z* [M+H]⁺ calc. for C₁₈H₁₃N₂O₃V is 356.0366, found 356.0314 (Fig. S5).

4.4 Synthesis of marigold flower shaped Ni₃V₂O₈ structure

VO(II) 8-Hydroxyquinoline and Ni(II) 8-Hydroxyquinoline complex were first dissolved in 2:3 molar ratio in 16 mL methanol which was further diluted to 36 mL by the addition of 20 mL double distilled water. The obtained solution was transferred into a Teflon-lined stainless-steel autoclave and heated at 220°C for 32h. The temperature was raised to 220°C with 10°C min⁻¹ heating rate. After the completion of the reaction, the heating was stopped and the hydrothermal autoclave was allowed to cool down naturally to room temperature. The precipitate was washed by centrifugation with methanol and DDW several times to remove the unreactive species. The Ni₃V₂O₈ flower product thus obtained was dried in a hot air oven at 70°C for 12h and finally stored for further studies.

4.5 Synthesis of V₂O₅ and NiO structure

For the preparation of pure V₂O₅ or NiO, a process similar to that followed for the synthesis of Ni₃V₂O₈ was carried out, except that [VO(Hq)₂] or [Ni(Hq)₂] complex was not subsist in the reactions medium. We have also prepared a physical mixture of V₂O₅ and NiO in equimolar ratio for OER performance.

4.6. Instrumentation

The structures of the compounds were determined by nuclear magnetic resonance spectroscopy and other spectroscopic

techniques. The NMR spectra were recorded with 500 MHz Bruker instruments. Chemical shifts are reported in δ values relative to the solvent peaks. The solvents used for the spectroscopy experiments were brought from Cambridge isotope laboratories. The mass spectrometric data were obtained from an Acquity TM Ultra Performance LC-ESI/quadruple-TOF MS. UV-Vis measurements were performed with a UV-Vis spectrophotometer (Shimadzu), ATR-FTIR was carried out using Bruker (Model: Vertex 70v) ATR spectrometer. The Field-emission scanning electron microscopy (FE-SEM) images were taken using Carl Zeiss (Merlin compact, 2014) FE-SEM. The transmission electron microscopy (TEM) images were taken using a JEOL-2100 transmission electron microscope with an operating voltage of 200 kV. The crystalline structures and phases were studied by X-ray diffraction pattern measurements which were done with Bruker Eco D8 advance X-ray powder diffractometer using Ni-filtered with Cu Kα radiation λ=1.54056 Å. The data was collected from 10° < 2θ < 80° with an increment of 0.019°. The high-resolution X-ray photoelectron spectroscopy (XPS) measurements were performed using the Thermo Scientific Inc. system equipped with a microfocus monochromatic Al Kα X-ray source of energy ~1450 eV. Brunauer-Emmett-Teller (BET) measurement was carried out with Make-QuantaChrome instruments, Model: AutosorbIQ and ASIQwin. All the electrochemical measurements were performed using Metrohm Autolab (Multichannel-204) connected to a standard three-electrode system using Nova 2.1.4 software.

4.7 Fabrication of working electrode

Catalyst inks were prepared by dissolving 3 mg of the catalyst in 0.68 mL of double distilled water and 0.4 mL of ethanol in a 1.5 mL micro centrifuge tube. This mixture was sonicated for 30 minutes prior to addition of 20 μL 5% Nafion solution, then further sonicated for another 15 min. The as-prepared 5 μL catalyst ink was drop casted on to the glassy carbon (GC) electrode and left overnight in vacuum desiccator for drying. The dried electrode is the used as working electrode (WE) for the study of oxygen evolution reaction (OER) activity and the mass loading of catalyst kept as 0.19 mg cm⁻². All the electrochemical experiments are performed at the room temperature.

For the electrochemical characterizations Ag/AgCl (3M KCl) and platinum (Pt) electrode were used as reference and counter electrode, respectively. Here, GC (3 mm diameter) electrode loaded with catalyst served as working electrode. All the experiments were carried out in 1M KOH (pH 13.8) solution prepared using DDW. The linear sweep voltammetry (LSV) was carried out in potential range of 0 V to 1 V vs. Ag/AgCl with a scan rate of 10 mV s⁻¹ and cyclic voltammetry (CV) experiments were carried in the potential range of 0.1V to 0.3 V (vs. Ag/AgCl) with scan rate varying from 20 mV s⁻¹ to 100 mV s⁻¹. The long-term stability of the catalyst was tested using chronoamperometric method by applying a constant overpotential of 369 mV for 10h. Further, stability of the Ni₃V₂O₈ catalyst was also studied by observing the change

in overpotential after contentious running of 2000 LSV cycles at a constant scan rate of 50 mV s⁻¹. Electrochemical impedance spectroscopy (EIS) was recorded at frequencies from 100 kHz to 0.1 Hz at 350 mV (vs. Ag/AgCl) in 1 M KOH solution. All the electrochemical measurement data, the potential with respect to RHE were converted using the following Nernst equation:

$$E_{(\text{RHE})} = E_{(\text{Ag}/\text{AgCl})} + 0.059\text{pH} + E_{\text{Ref}}$$

5. Conclusion

In summary, we fabricated the Marigold flower shaped structure of Ni₃V₂O₈ which is an unique morphology that was obtained by a single step hydrothermal synthesis method via thermal decomposition of [Ni(Hq)₂] and [VO(Hq)₂] complexes. In this synthesis, many factors have been tested and are accounted for achieving the Marigold flower shaped Ni₃V₂O₈ structure. We have shown that Marigold flower shaped Ni₃V₂O₈ exhibit magnificent electrochemical properties (compared to other spinel oxides, Table S2) as the potential electrode materials for OER. The marigold flower shaped Ni₃V₂O₈ structure shows a good activity for OER with overpotential of 328 mV at 10 mA cm⁻² and Tafel slope of 61 mV dec⁻¹. The outstanding OER execution of marigold flower shaped Ni₃V₂O₈ structure is even comparable to that of commercial IrO₂ (overpotential 360 mV at 10 mA cm⁻² and Tafel slope of 65 mV dec⁻¹) electrocatalyst. The high electrocatalytic activity of Ni₃V₂O₈ can be attributed to the synergetic effect between variable oxidation state of V and Ni metal ions. Results presented here propose that with legitimate control and engineered chemical reaction; more suitable and active composite nanostructure can be planned and utilized as profoundly productive electrocatalyst for oxygen evolution reaction.

Conflicts of interest

There are no conflicts to declare.

Acknowledgements

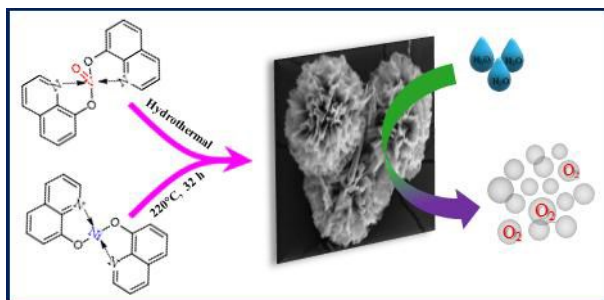
This work was financially supported by the Department of Science and Technology, DST (Project No. EEQ/2017/000467) is gratefully acknowledged. The paper was written through contributions of all authors. R.B. is thankful to the DST for providing INSPIRE fellowship for Ph.D. programme (DST/INSPIRE Fellowship/[IF190052]). All authors have given approval to the final version of the paper.

References

- F. Cheng and J. Chen, *Chem. Soc. Rev.*, 2012, **41**, 2172-2192.
- Y. Bing, H. Liu, L. Zhang, D. Ghosh and J. Zhang, *Chem. Soc. Rev.*, 2010, **39**, 2184-2202.
- T. E. Mallouk, *Nat. Chem.*, 2013, **5**, 362-363.
- M. K. Debe, *Nature*, 2012, **486**, 43-51.
- A. J. Esswein, M. J. McMurdo, P. N. Ross, A. T. Bell and T. D. Tilley, *J. Phys. Chem. C*, 2009, **113**, 15068-15072.
- Y. Meng, W. Song, H. Huang, Z. Ren, S.-Y. Chen and S. L. Suib, *J. Am. Chem. Soc.*, 2014, **136**, 11452-11464.
- Z. Chen, B. Zhao, Y.-C. He, H.-R. Wen, X.-Z. Fu, R. Sun and C.-P. Wong, *Mater. Chem. Front.*, 2018, **2**, 1155-1164.
- C. Luan, G. Liu, Y. Liu, L. Yu, Y. Wang, Y. Xiao, H. Qiao, X. Dai and X. Zhang, *ACS Nano*, 2018, **12**, 3875-3885.
- X. Chen, H. Wang, R. Meng, B. Xia and Z. Ma, *ACS Appl. Energy Mater.*, 2020.
- A. S. Batchellor, G. Kwon, F. A. Laskowski, D. M. Tiede and S. W. Boettcher, *J. Phys. Chem. C*, 2017, **121**, 25421-25429.
- B. Mohanty, M. Ghorbani-Asl, S. Kretschmer, A. Ghosh, P. Guha, S. K. Panda, B. Jena, A. V. Krashenninnikov and B. K. Jena, *ACS Catal.*, 2018, **8**, 1683-1689.
- J. S. Chen, J. Ren, M. Shalom, T. Fellingner and M. Antonietti, *ACS Appl. Mater. Interfaces*, 2016, **8**, 5509-5516.
- A. M. Wiltrout, C. G. Read, E. M. Spencer and R. E. Schaak, *Inorg. Chem.*, 2016, **55**, 221-226.
- M. Chauhan, K. P. Reddy, C. S. Gopinath and S. Deka, *ACS Catal.*, 2017, **7**, 5871-5879.
- J.-Y. Zhang, L. Lv, Y. Tian, Z. Li, X. Ao, Y. Lan, J. Jiang and C. Wang, *ACS Appl. Mater. Interfaces*, 2017, **9**, 33833-33840.
- J. Masud, W. P. Liyanage, X. Cao, A. Saxena and M. Nath, *ACS Appl. Energy Mater.*, 2018, **1**, 4075-4083.
- S. Chen, J.-L. Mi, P. Zhang, Y.-H. Feng, Y.-C. Yong and W.-D. Shi, *J. Phys. Chem. C*, 2018, **122**, 26096-26104.
- Z. Fang, L. Peng, H. Lv, Y. Zhu, C. Yan, S. Wang, P. Kalyani, X. Wu and G. Yu, *ACS Nano*, 2017, **11**, 9550-9557.
- J. Chang, Y. Xiao, M. Xiao, J. Ge, C. Liu and W. Xing, *ACS Catal.*, 2015, **5**, 6874-6878.
- A. Dutta and N. Pradhan, *J. Phys. Chem. Lett.*, 2017, **8**, 144-152.
- K. Liu, C. Zhang, Y. Sun, G. Zhang, X. Shen, F. Zou, H. Zhang, Z. Wu, E. C. Wegener and C. J. Taubert, *ACS Nano*, 2018, **12**, 158-167.
- L. Li, X. Feng, Y. Nie, S. Chen, F. Shi, K. Xiong, W. Ding, X. Qi, J. Hu and Z. Wei, *ACS Catal.*, 2015, **5**, 4825-4832.
- L. Jin, X. Zheng, W. Liu, L. Cao, Y. Cao, T. Yao and S. Wei, *J. Mater. Chem. A*, 2017, **5**, 12022-12026.
- H. S. Jeon, M. S. Jee, H. Kim, S. J. Ahn, Y. J. Hwang and B. K. Min, *ACS Appl. Mater. Interfaces*, 2015, **7**, 24550-24555.
- R. I. Poulain, A. Klein and J. Proost, *J. Phys. Chem. C*, 2018, **122**, 22252-22263.
- P. Manivasakan, P. Ramasamy and J. Kim, *RSC Adv.*, 2015, **5**, 33269-33274.
- A. Samanta, S. Das and S. Jana, *ACS Sustainable Chem. Eng.*, 2019, **7**, 12117-12124.
- M. Müllner, M. Riva, F. Kraushofer, M. Schmid, G. S. Parkinson, S. F. Mertens and U. Diebold, *J. Phys. Chem. C*, 2018, **123**, 8304-8311.
- X. Liu, S. Cui, Z. Sun, Y. Ren, X. Zhang and P. Du, *J. Phys. Chem. C*, 2016, **120**, 831-840.
- S. K. Bikkarolla and P. Papakonstantinou, *J. Power Sources*, 2015, **281**, 243-251.
- D. U. Lee, B. J. Kim and Z. Chen, *J. Mater. Chem. A*, 2013, **1**, 4754-4762.
- Z. Li, B. Li, J. Chen, Q. Pang and P. Shen, *Int. J. Hydrogen Energy*, 2019, **44**, 16120-16131.
- H. Yang, Y. Liu, S. Luo, Z. Zhao, X. Wang, Y. Luo, Z. Wang, J. Jin and J. Ma, *ACS Catal.*, 2017, **7**, 5557-5567.

34. C. Si, Y. Zhang, C. Zhang, H. Gao, W. Ma, L. Lv and Z. Zhang, *Electrochim Acta*, 2017, **245**, 829-838.
35. T. W. Kim, M. A. Woo, M. Regis and K.-S. Choi, *J. Phys. Chem. Lett.*, 2014, **5**, 2370-2374.
36. M. Li, Y. Xiong, X. Liu, X. Bo, Y. Zhang, C. Han and L. Guo, *Nanoscale*, 2015, **7**, 8920-8930.
37. X. Ge, Y. Liu, F. T. Goh, T. A. Hor, Y. Zong, P. Xiao, Z. Zhang, S. H. Lim, B. Li and X. Wang, *ACS Appl. Mater. Interfaces*, 2014, **6**, 12684-12691.
38. T. Y. Ma, Y. Zheng, S. Dai, M. Jaroniec and S. Z. Qiao, *J. Mater. Chem. A*, 2014, **2**, 8676-8682.
39. M.-C. Liu, L.-B. Kong, L. Kang, X. Li, F. C. Walsh, M. Xing, C. Lu, X.-J. Ma and Y.-C. Luo, *J. Mater. Chem. A*, 2014, **2**, 4919-4926.
40. Y. Shang, T. Xie, Y. Gai, L. Su, L. Gong, H. Lv and F. Dong, *Electrochim Acta*, 2017, **253**, 281-290.
41. V. Soundharrajan, B. Sambandam, J. Song, S. Kim, J. Jo, D. T. Pham, S. Kim, V. Mathew and J. Kim, *Ceram. Int.*, 2017, **43**, 13224-13232.
42. B. Sambandam, V. Soundharrajan, J. Song, S. Kim, J. Jo, D. T. Pham, S. Kim, V. Mathew, K. H. Kim and Y.-K. Sun, *J. Electroanal. Chem.*, 2018, **810**, 34-40.
43. F. Liu, R. Sun, Y. Guan, X. Cheng, H. Zhang, Y. Guan, X. Liang, P. Sun and G. Lu, *Sens. Actuators, B*, 2015, **210**, 795-802.
44. C. Wang, D. Fang, Y. Cao, W. Xu, X. Liu, Z. Luo, G. Li, M. Jiang and C. Xiong, *Sci. Rep.*, 2016, **6**, 20826.
45. M. Masalovich, L. Ardasheva and G. Shagisultanova, *Russ. J. Inorg. Chem.*, 2006, **51**, 1498.
46. K. E. Yorov, A. Yapryntsev, A. Baranchikov, T. Khamova, E. Straumal, S. Lermontov and V. Ivanov, *J. Sol-Gel Sci. Technol.*, 2018, **86**, 400-409.
47. W. Pelzold, *Angew. Chem.*, 1958, **70**, 277-278.
48. M. L. Ramos, L. L. Justino, S. M. Fonseca and H. D. Burrows, *New J. Chem.*, 2015, **39**, 1488-1497.
49. I. Gryca, K. Czerwińska, B. Machura, A. Chrobok, L. S. Shul'pina, M. L. Kuznetsov, D. S. Nesterov, Y. N. Kozlov, A. J. Pombeiro and I. A. Varyan, *Inorg. Chem.*, 2018, **57**, 1824-1839.
50. R. R. Langeslay, D. M. Kaphan, C. L. Marshall, P. C. Stair, A. P. Sattelberger and M. Delferro, *Chem. Rev.*, 2018, **119**, 2128-2191.
51. C. Engelter, G. E. Jackson, C. L. Knight and D. A. Thornton, *J. Mol. Struct.*, 1989, **213**, 133-144.
52. R. D. Shannon, D. B. Rogers and C. T. Prewitt, *Inorg. Chem.*, 1971, **10**, 713-718.
53. D. E. Hamilton, *Inorg. Chem.*, 1991, **30**, 1670-1671.
54. W. J. Pietro, M. M. Francl, W. J. Hehre, D. J. DeFrees, J. A. Pople and J. S. Binkley, *J. Am. Chem. Soc.*, 1982, **104**, 5039-5048.
55. D. A. Thornton, *Vib. Spectrosc.*, 1993, **4**, 309-319.
56. M. L. Ramos, L. L. Justino, A. Branco, C. M. Duarte, P. E. Abreu, S. M. Fonseca and H. D. Burrows, *Dalton Trans.*, 2011, **40**, 11732-11741.
57. J. Kidrič, D. Hadži, D. Kocjan and V. Rutar, *Org. Magn. Reson.*, 1981, **15**, 280-284.
58. Y.-L. Chan, S.-Y. Pung and S. Sreekantan, *J. Catal.*, 2014, **2014**.
59. S. Vijayakumar, S. Nagamuthu and G. Muralidharan, *ACS Appl. Mater. Interfaces*, 2013, **5**, 2188-2196.
60. Z. Wang, G. M. Kale, Q. Yuan and M. Ghadiri, *RSC Adv.*, 2012, **2**, 9993-9997.
61. H. Fuess, E. Bertaut, R. Pauthenet and A. Durif, *Acta Crystallogr., Sect. B: Struct. Crystallogr. Cryst. Chem.*, 1970, **26**, 2036-2046.
62. R. Kumar, P. Rai and A. Sharma, *J. Mater. Chem. A*, 2016, **4**, 9822-9831.
63. N. McIntyre and M. Cook, *Anal. Chem.*, 1975, **47**, 2208-2213.
64. B. M. Reddy, P. M. Sreekanth, E. P. Reddy, Y. Yamada, Q. Xu, H. Sakurai and T. Kobayashi, *The J. Phys. Chem. B*, 2002, **106**, 5695-5700.
65. X. Yang, F. Ma, K. Li, Y. Guo, J. Hu, W. Li, M. Huo and Y. Guo, *J. Hazard. Mater.*, 2010, **175**, 429-438.
66. Q. Zhao, Z. Yan, C. Chen and J. Chen, *Chem. Rev.*, 2017, **117**, 10121-10211.
67. N.-T. Suen, S.-F. Hung, Q. Quan, N. Zhang, Y.-J. Xu and H. M. Chen, *Chem. Soc. Rev.*, 2017, **46**, 337-365.
68. K. Nakamoto and N. Ohkaku, *Inorg. Chem.*, 1971, **10**, 798-805.

Table of Contents (TOC)



$\text{Ni}_3\text{V}_2\text{O}_8$ flowers designed by a thermal decay of molecular precursors show excellent OER activity with an overpotential of 328 mV.